

Spin and valley filter based on two-dimensional WSe₂ heterostructures

D. Zambrano, P. A. Orellana, and L. Rosales

Departamento de Física, Universidad Técnica Federico Santa María, Casilla 110-V, Valparaíso, Chile.

A. Latgé*

Instituto de Física, Universidade Federal Fluminense, Niterói-RJ, Brazil.

(Dated: January 6, 2022)

In this work, we investigate spin and valley transport properties of a WSe₂ monolayer placed on top of a ferromagnetic insulator. We are interested in controlling the transport properties by applying external potentials to the system. To obtain spin and valley polarizations, we have considered a single and a double barrier structure with gate potentials. We have analyzed how the efficiency of these polarized transport properties depend on the gate-potential intensities and geometrical configurations. Additionally, we investigate how the spin and valley transport properties are modified when an ac-potential is applied to the system. We have obtained a controllable modulation of the spin and valley polarizations as a function of the intensity and frequency of the ac-potential, mainly in the terahertz range. These results validate the proposal of double quantum well structures of WSe₂ as candidates to provide spin and valley dependent transport within an optimal geometrical parameter regime.

I. INTRODUCTION

Transition metal dichalcogenides (TMDCs) play an important role in nanotechnology nowadays due to their novel physical and chemical properties [1–8]. Compared with graphene, they have the great advantage of presenting electronic gaps in a wide size range within the visible and infrared spectra. Examples of TMDCs are tungsten disulfide (WS₂), molybdenum diselenide (MoSe₂), tungsten diselenide (WSe₂), and molybdenum disulfide (MoS₂) [9–18]. These materials have been considered for many technological applications in electronic [19, 20] and optoelectronic [21–23], as gas sensing [24] devices, ultra-sensitive photodetectors [25], among others [9–12, 26, 27]. In particular, the TMDCs monolayer of group VI present a direct bandgap in the optical range suggesting possible applications in optoelectronics devices. In this context, TMDCs have emerged as excellent candidates of ultra-thin semiconductor materials, with a tunable bandgap in the optical region [6, 19]. Moreover, the application of appropriate gate voltages and the presence of magnetic materials to induce magnetic proximity effects have been explored, revealing the different mechanisms of tailoring electronic properties [28].

Electronic transport properties of TMDCs and their possible applications are determined by the corresponding carrier mobility and spin and valley carriers mean free path [7]. There are several challenging proposals involve the possibility of spin and valley filtering within spintronic and valleytronic scenarios[29] The theoretically predicted values for the charge mobility are promising, but, of course, limited by intrinsic scattering processes such as phonon scattering or local Coulomb potentials induced by impurities [5–8, 19]. Besides, Spin-orbit coupling induced valley Hall effects were reported on TMD

materials and addressed as a manifestation of applied gate voltage[30]. This type of induced valley Hall effects was attributed to a coexistence of Ising and Rashba spin-orbit coupling in gated/polar TMDCs originated from inversion-asymmetric spin-orbit interactions.

Although most of the studies on transport properties of TMDCs systems have been made in the *dc* regime, interesting quantum transport phenomena appear when external time-dependent fields perturb these materials. Comparing with stationary potentials, a time-varying one can effectively modulates the quantum phase of the electronic wave functions [31–33], bringing new possibilities for technological devices. Single-electron pumps were designed applying a time-dependent gate voltage in quantum systems [34] and radio frequency analog electronic devices were synthesized based on carbon nanotube (CNT) transistors [35]. Others interesting effects are the photon-assisted tunneling in graphene bilayers [36], *ac*-field effects on the conductance and noise of CNT and graphene nanoribbon devices in the Fabry Perot regime [37, 38], quantum charge pumping in carbon-based devices [39], and irradiated graphene as a tunable Floquet topological insulator [40].

In TMDCs, the photon-assisted transport response has been lesser reported in comparison with other materials. For instance, the electric behavior of a mechanically exfoliated MoS₂ single-layer based phototransistor [41] was investigated. The photocurrent generation was found to depend solely on the illuminating optical power at a constant drain or gate voltage, exhibiting better photoresponsivities than those proposed in the graphene-based device. Hybrid TMDCs photoelectronic devices, based on graphene-MoS₂, have been proposed[42] as a possible application in multifunctional photoresponsive memory devices. Also, photocurrent was found at zero bias voltage [43] in *p* – *n* vertical junction formed by a hybrid system of WSe₂/MoS₂, as the system is irradiated by a 514 nm laser (5 μ W). Studies of the influence of

* alatge@id.uff.br

an optical field on spin and valley polarized transport of WSe₂ monolayer were recently reported taking into account also the effects of a Fermi velocity barrier[44]. All these reports undoubtedly suggest that photon-assisted phenomena can be an additional mechanism of controlling transport in TMDCs nanostructures.

With the above motivations, here we investigate the possibility of inducing and controlling spin and valley polarizations on different potential profiles of 2D-WSe₂ heterostructures. We have studied the case of a single and a double potential barrier configurations. We focused on the resonant regime and how this effect allows the spin and valley polarizations. Exchange valley splitting was provided by magnetic proximity effect with the advantageous that the splitting is dictated by the exchange interaction strength and no applied magnetic field is need. This allows a convenient scenario for obtaining tunneling processes. Moreover, due to the versatility of being either positive or negative valued this description opens the possibility of tuning valley splitting sign and magnitude together. Furthermore, we have analyzed the possibility of promoting valley and spin polarization inversions on TMDCs layers under the effects of time-dependent external potentials, such as time-oscillating gate voltages or laser radiation. Different mechanisms are analyzed to synchronize the proposed system's physical parameters, such as Fermi energy, frequency and amplitude of the time-dependent potential, and external gate voltages, to optimize time-dependent transport properties, such as induced switching effects of the transport of the systems.

II. THE MODEL

The proposed device consists of a WSe₂ monolayer partially placed over a ferromagnetic insulator (EuS), as it is schematically depicted in Fig. 1. The whole system is composed of three regions: two leads, modeled by pristine regions of WSe₂ and a central conductor at which a ferromagnetic insulator is fixed under the WSe₂ layer. In order to modulate the transport response of the system, we have considered top gate potentials in different configurations, forming two distinct heterostructures: i) a single barrier and b) a double barrier. In the case of a single barrier, a top gate is placed over the finite region of the central conductor, whereas for the double barrier configuration, three different top gates are used to define this system, as it is marked in yellow/green in Fig.1

The Hamiltonian describing the 2D system of interest can be written as:

$$H = H_0 + H_{\text{ex}} + H_g + H_{\text{ac}}, \quad (1)$$

where H_0 is an effective Hamiltonian, written in the continuum model as discussed in previous works [1, 2], which adjusts well with DFT calculations. This is a convenient approach to study transport response near the Fermi energy. The term H_{ex} represents the exchange field induced

by the interaction of the WSe₂ layer with the EuS ferromagnetic insulator, that promotes an energy exchange splitting as a magnetic proximity effects. The two last terms correspond to an external gate voltage H_g , that can spatially modulate tunneling and resonance features and H_{ac} is a time-dependent potential.

In the low energy approximation, the effective Hamiltonian is written as,

$$H_0 = v_F (\eta \sigma_x p_x + \sigma_y p_y) + \frac{m}{2} \sigma_z + \eta S_z (\lambda_c \sigma_+ + \lambda_v \sigma_-). \quad (2)$$

where v_F is the electronic Fermi velocity and $\eta = \pm 1$ reads for K and K' valleys. The second term is the mass term which breaks the inversion symmetry and $S_z = \pm 1$ is the spin index. The parameters $\lambda_{c,v}$ give the spin-splitting of the conduction and valence bands, respectively, and is due to intrinsic spin-orbit coupling, and:

$$\sigma_{\pm} = \frac{1}{2} (\sigma_0 \pm \sigma_z), \quad (3)$$

with σ_0 denoting the identity matrix. The exchange term, following Norden *et. al.* [1] and Qi *et. al.* [2], is written as:

$$H_{\text{ex}} = -S_z (B_c \sigma_+ + B_v \sigma_-). \quad (4)$$

where $B_{c,v}$ may be interpreted as an effective Zeeman field experienced by the conduction and valence bands of the WSe₂ due to the proximity with the ferromagnetic substrate. It is important to mention that the Norden model parameters are based on DFT calculations to reproduce the exact band structures of WSe₂ in the low energy regime.

The external gate voltage term is defined as

$$H_g = U(x), \quad (5)$$

where $U(x)$ represents a sequence of potential barriers and well which define an heterostructure device, as it is illustrated schematically in Fig. 1, for the case of a double barrier system. We have denoted the barrier length as L and the potential barrier height as U_b , whereas, the well length is taken as d and the potential well deep is given by U_w . Finally, the time-dependent Hamiltonian term is given by $H_{\text{ac}} = eV(t) = V_{\text{bias}} \cos(\omega t)$, where V_{bias} and ω represent the ac-potential intensity and the frequency, respectively. It is important to mention that, following the Tien-Gordon approach [45], this term has been applied to the whole system.

In our model we have not included the Rashba interaction in the Hamiltonian, considering the exchange coupling more relevant in our approach. In the calculation, we are interested in the electronic transport through the conduction band that presents an energy splitting greater than the usual Rashba term [30].

We have considered the cases of a single barrier and a double barrier potential profile. The electronic transmission through the conductor region is calculated following

the same scheme, in both configurations, as is described in Appendix A. The transmission coefficient of the single barrier $t_{\eta, S_z}^{\text{single}}$, can be analytically determined, and is given by:

$$t_{S_z, \eta}^{\text{Single}} = \frac{2}{\xi} \cos(\theta) \cos(\varphi) e^{-ik_x L}, \quad (6)$$

where the term ξ is defined as:

$$\begin{aligned} \xi = & \cos(\theta - \varphi) e^{iq_x L} + \cos(\theta + \varphi) e^{-iq_x L} \\ & - i \left(\frac{c_k b_q}{c_q b_k} + \frac{c_q b_k}{c_k b_q} \right) \sin(q_x L), \end{aligned} \quad (7)$$

with $\theta = \arctan(\frac{k_y}{k_x})$, $\varphi = \arctan(\frac{k_y}{q_x})$, $k_{x,y}$ and $q_{x,y}$ are the wave vector components of the electron outside and inside the barrier, respectively, and c_k, c_q, b_k, b_q are amplitude coefficients of the electronic wave function outside and inside the barrier, defined in the Appendix A. It is also possible to obtain an analytic expression for the double barrier transmission coefficient $t_{S_z, \eta}^{\text{Double}}$, derived in the Appendix in Eq. (A16).

For both cases ($t_{S_z, \eta}^{\text{Single}}$ and $t_{S_z, \eta}^{\text{Double}}$) the angular dependent transmission probability $T_{S_z, \eta}(\theta)$ is defined as:

$$T_{S_z, \eta}(\theta) = |t_{S_z, \eta}|^2, \quad (8)$$

while the spin- and valley- conductance are written as:

$$\mathcal{G}_{S_z, \eta} = \int_{-\pi/2}^{\pi/2} T_{S_z, \eta} \cos(\theta) d\theta. \quad (9)$$

We discuss further the effects of an ac-potential of frequency ω and intensity V_{ac} on the transport properties

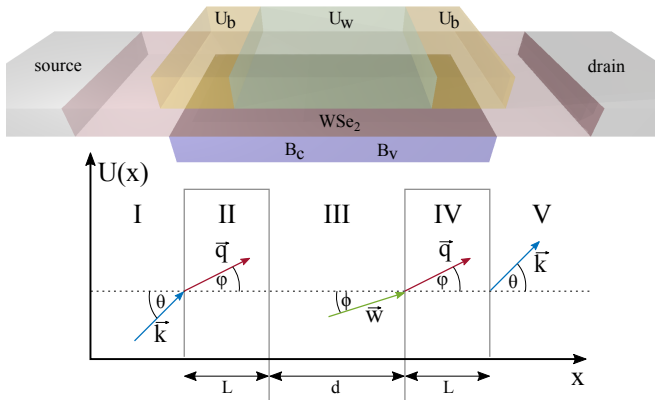


FIG. 1. Schematic view of a WSe₂ double barrier heterostructure. Zones II and IV are the potential barriers of length L and height U_b . Region III is the well with length d and depth U_w . In zones II, III and IV the presence of the substrate provides the exchange potentials B_c and B_v .

of the proposed device. Following the Tien-Gordon formalism [45], the spin- and valley- conductance may be written as [36]

$$G_{S_z, \eta} = G_0 \sum_{m=-\infty}^{\infty} J_m^2 \left(\frac{eV_{ac}}{\hbar\omega} \right) \mathcal{G}_{S_z, \eta}(\varepsilon_f + m\hbar\omega), \quad (10)$$

where J_m are the Bessel functions of first kind.

Here we use the spin dependent conductance as:

$$G_{\uparrow(\downarrow)} = G_{\uparrow(\downarrow)K} + G_{\uparrow(\downarrow)K'}, \quad (11)$$

and the valley dependent conductance as:

$$G_{K(K')} = G_{\uparrow K(K')} + G_{\downarrow K(K')}. \quad (12)$$

Following standard definitions, the valley-polarized conductance is written as

$$P_v = \frac{G_K - G_{K'}}{G_K + G_{K'}}, \quad (13)$$

whereas the spin-polarized conductance as

$$P_s = \frac{G_{\uparrow} - G_{\downarrow}}{G_{\uparrow} + G_{\downarrow}}. \quad (14)$$

In what follows, we discuss the results for spin and valley polarizations obtained for both single and double barrier heterostructure systems, considering different mechanisms to modulate the transport response of the proposed device.

III. RESULTS

The low energy band structures for the WSe₂ heterostructure are presented in Fig. 2 considering the three regions: leads, barriers and well. We adopt, for simplicity, the notation of K_+ and K_- , for the traditional K and K' valleys. Red and blue curves denote the spin up and down bands that, due to the symmetries of WSe₂, are inverted for K_+ and K_- valleys. To obtain these band structures, we have used the following parameter values: $\lambda_c = 34.20$ meV, $\lambda_v = 418.05$ meV, $B_c = 18.20$ meV, $B_v = 13.75$ meV, and $m = 1558.70$ meV [1]. The lattice constant is $a_0 = 0.3316$ nm and the Fermi velocity $v_f = 5.30 \times 10^{14}$ nm/s.

The energy split induced by the ferromagnetic substrate (B_c and B_v) for the well and barrier regions, is marked with dashed black lines in the electronic band structures presented in Fig. 2 b) and c). The energy split $\Delta E = 36.40$ meV matches the ones reported in Fig. 7 of Ref. [1]. The energy axis has been redefined as $E - E_{bott}$ where $E_{bott} = 745.15$ meV is the bottom energy of the conduction bands in the leads. The horizontal black lines in the three panels of Fig. 2 represent the incoming electron energy level, which is 104.68 meV (175.10 meV) above the Fermi level for the double (single) barrier system. Energy values up to 400 meV were

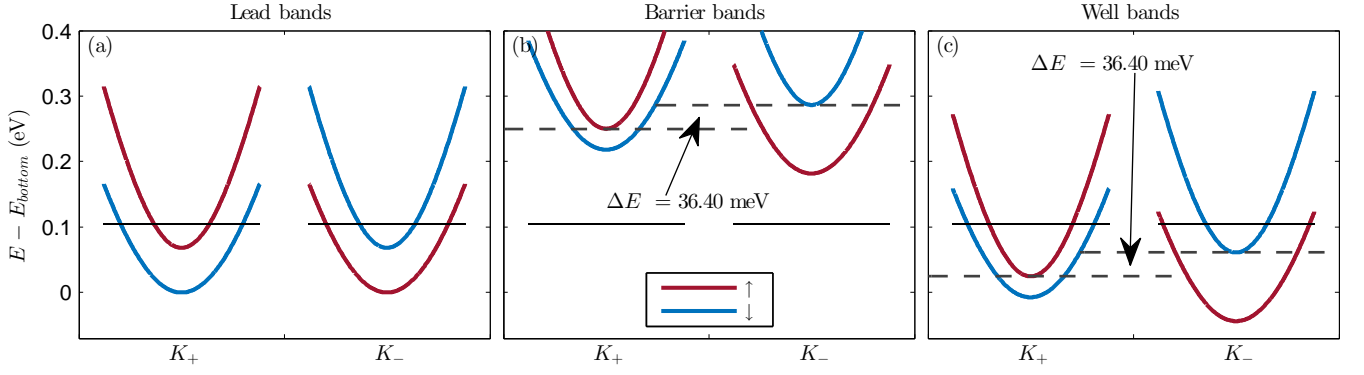


FIG. 2. Band structures of a WSe₂ heterostructure corresponding to: (a) the leads, (b) barrier region and (c) well region composing a double barrier system (in a single barrier system panel (c) is neglected). The bottom of the lead conduction band has been redefined as the zero energy. Solid black lines show the energy of the incoming electron. Dashed black lines in (b) and (c) define the energy difference between the bottom of the spin-up conduction band in the valley K_+ and the spin-down conduction band in the valley K_- .

considered for the potential U_b of the double barrier systems, that are chosen in a symmetric configuration. In the case of single barrier systems, U_b takes values up to 200 meV. For the well potential U_w values up to 100 meV were considered. In this context, it is possible to observe in panels b) and c) of Fig. 2 how the spin bands are displaced as the potentials U_b and U_w are applied in the system.

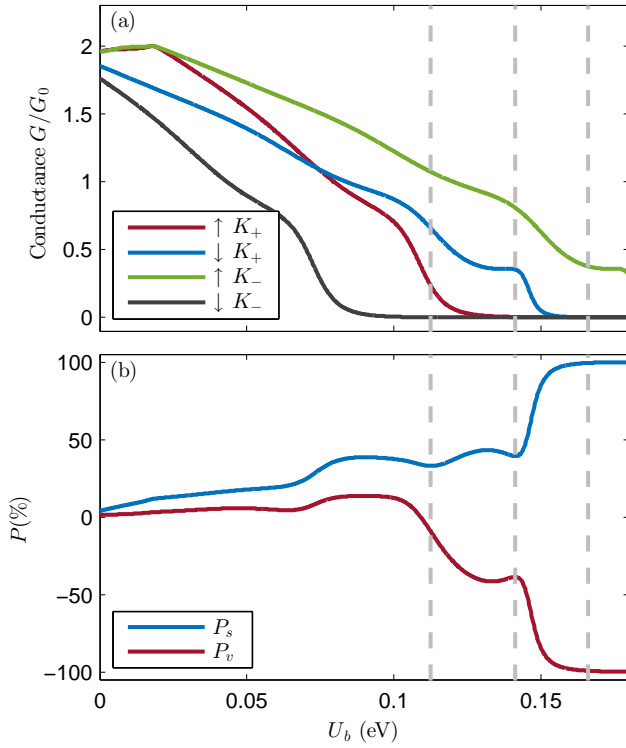


FIG. 3. Spin and valley conductances (a) and polarizations (b) as a function of the barrier height U_b for the single barrier system, with barrier length $L = 20$ nm. Both panels are at energy 175.10 meV above the Fermi level.

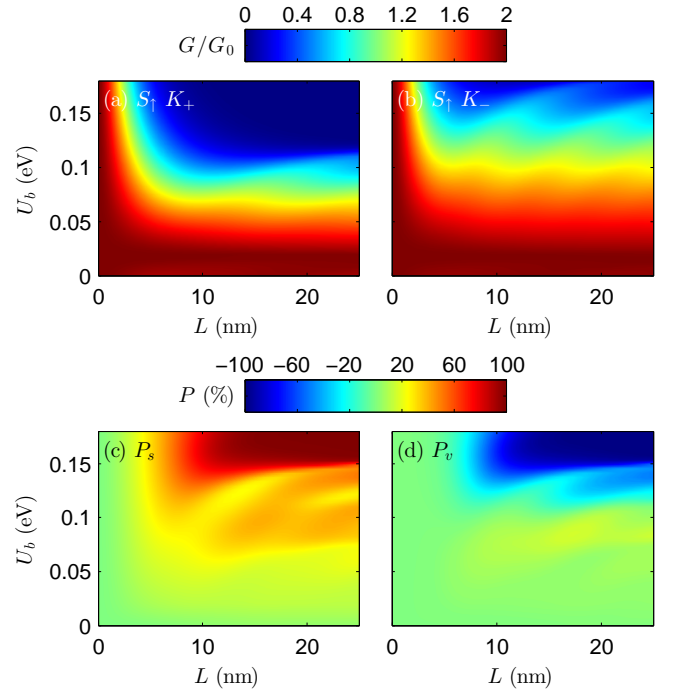


FIG. 4. (a) $S\uparrow K_+$ conductance component, (b) $S\uparrow K_-$ conductance component and (c) spin and (d) valley polarization contour plots, for a single barrier system, as functions of the barrier height U_b and length L , at a fixed energy of 175.10 meV above the Fermi level.

We discuss first the cases of single and double barrier heterostructures in the absence of the time-dependent term, presented in Eq. 1. The ac-field contribution is only taken into account in subsection (C) where a double-barrier system is revisited under the effects of a time-dependent radiation.

A. Single Barrier

Results of spin and valley resolved conductance and polarization, as a function of the single barrier potential energy, are presented in Fig. 3 (a) and (b). Here we have chosen a barrier length $L = 20$ nm and an incident electron energy $E = 175.10$ meV above the Fermi level. The four spin and valley conductance components are denoted as $\uparrow K_+$, $\downarrow K_+$, for the valley K_+ and as $\uparrow K_-$ and $\downarrow K_-$, for the K_- . All conductance curves fall down, as it is expected, as the barrier height increases blocking the electronic transport. The corresponding spin and valley polarizations, given by blue and red curves respectively, depend strongly on the barrier height, as it is shown in Fig.3(b). It is important to note that the polarization is not very pronounced when the four conduction channels are active, mainly the valley polarization. However, as the conductance starts falling down, the polarization is enhanced, achieving maximum values when there is just a single conduction channel (green curve in Fig. 3(a)). Particular potential values ($0.16 < U_b < 0.20$) predict total polarized spin and valley configurations. A full spin and valley filter can be achieved then in this single barrier heterostructure.

We wonder about how robust this spin and valley filter are as a function of the barrier length and the range of potential intensities that we have used. In Fig. 4 we show contour plots of: (a) $\uparrow K_+$ and (b) $\uparrow K_-$ conductance components, (c) spin polarization P_s and (d) valley polarization P_v as functions of the barrier height U_b and length L , at a fixed energy of 175.10 meV above the Fermi level. In panels (a) and (b) it is possible to observe that the $\uparrow K_+$ and $\uparrow K_-$ conductance components behave uniformly as the barrier length is increased over 5 nm, diminishing they values as the potential intensity U_b is higher. However, there is a different potential intensity at which these two components become zero, around 0.1 eV for $\uparrow K_+$ and 0.15 eV for $\uparrow K_-$ respectively. Considering the equations 14 and 13, it is possible to obtain a perfect spin and valley filters in a wide range of parameters, as it is reflected in panel (c) and (d) of Fig. 4. Thus, single barrier heterostructures larger than 10 nm and with potential energy range between 140 – 200 meV are appropriated to obtain spin and valley filters, as it is indicated by red and blue regions in both polarization contour plots. These results give a guideline to choice single barrier WSe₂ heterostructures that would behave as filter.

B. Double Barrier

In what follows, we explore different configurations for the top gate voltages applied to the WSe₂ monolayer that transform the system into semiconducting quantum well heterostructures. Results for the spin and valley conductances and polarizations as a function of the well potential energy are shown in Fig. 5 and Fig. 7 for a

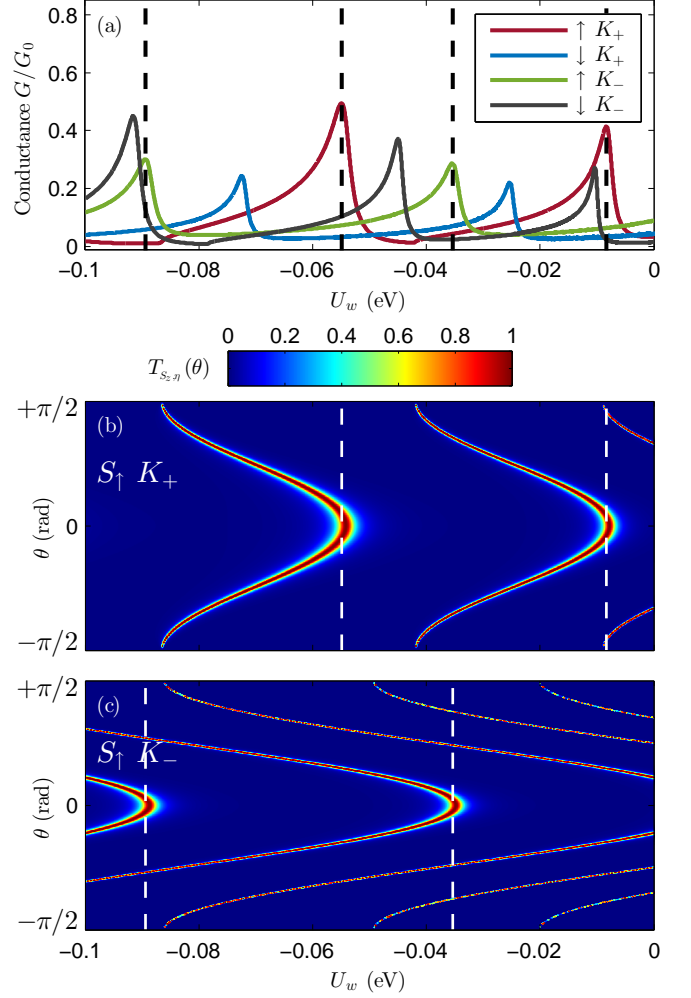


FIG. 5. (a) Spin and valley conductance as a function of the well depth for a double barrier system. Barrier length $L = 3$ nm, well length $d = 30$ nm, and barrier height $U_b = 300$ meV. (b-c) Transmission as a function of the incident angle θ . White dashed lines correspond to the peaks of the conductance components shown in panel (a) with black dashed lines. All panels are at 104.68 meV above the Fermi level

symmetric double barrier device. The left and right barrier lengths and potentials are equal to $L = 3$ nm and $U_b = 300$ meV, respectively. Although apparently small, such a size barrier corresponds to around 10 atomic layers, which is experimentally feasible nowadays[46]. The well length is fixed and equal to $d = 30$ nm. Unlike the tunneling phenomena observed in the single barrier case, resonant states are typical for double barrier profiles, which define the transport behavior of this kind of resonant systems. The states may be tuned, for instance, by changing the well potential depth. This is evidenced in the sequence of conductance peaks depicted in Fig. 5 (a). The features of the spin and valley components of the conductance are similar, although shifted in relation to the potential depth. This is understood by the alignment of the allowed conduction channels inside of the

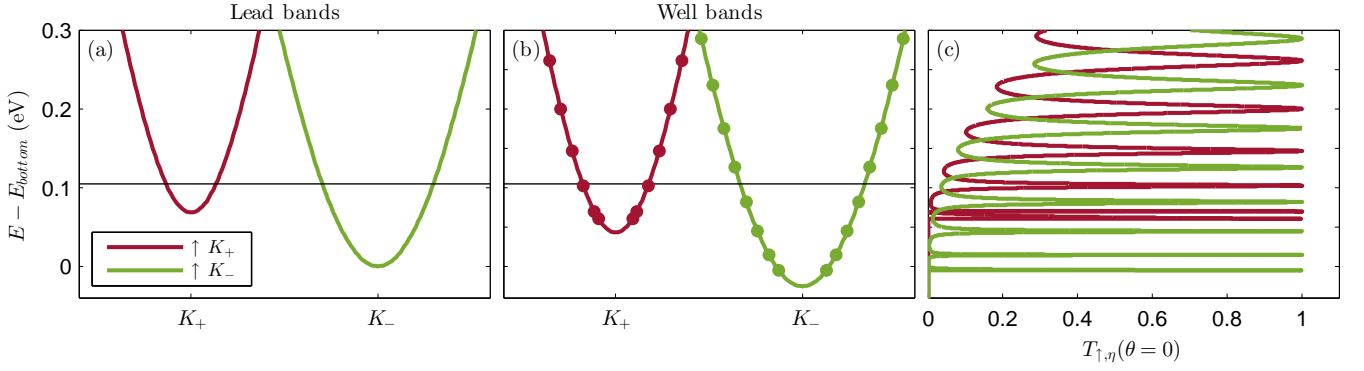


FIG. 6. (a-b) Lead and well bands (spin up), for the case of a double barrier system with barrier and well lengths $L = 3$ nm and $d = 30$ nm, respectively, barrier height $U_b = 300$ meV and well depth $U_w = -25.40$ meV. The energy of the incoming electron, chosen as 104.68 meV above the Fermi level, is marked as black horizontal lines. (c) Spin-valley transmission as a function of the incoming electron energy for the double barrier system, in the case of normal incident angle $\theta = 0$.

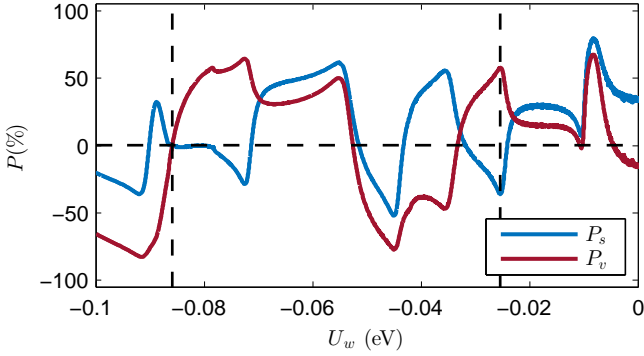


FIG. 7. Spin and valley polarizations as a function of the well depth for the double barrier system. Barrier length $L = 3$ nm, well length $d = 30$ nm, and barrier height $U_b = 300$ meV at 104.68 meV above the Fermi level. Vertical dashed lines in panel are drawn at $U_w = -85.9$ meV and at -25.4 meV.

well region (defined by the well length) and the incident electron energy, as the potential U_w is modified (see Fig. 2).

It is important to note that the conductance peak values associated with the resonant states do not attain its maximum. The presence of evanescent states and energy level changes due to the exchange coupling may be some of the reasons. Another important contribution comes from the angular dependence of the transmission, as illustrated in Fig. 5 (b) and (c). Partial maximum conductance values at particular U_w denoted by dashed lines in panel (a) do exhibit maximum transmission but restricted to a finite angular range as explicitly shown in panels (b) and (c), leading to demoted conductance lesser than one quantum conductance. In fact, we can also observe that the transmission probability takes high values for angles around the normal incidence of the carriers. The sequence of conductance peaks allows a rich variety of spin and valley polarization dependence on the well depth, as shown in fig. 5(b), that may be explored.

The band alignments of the leads and well, and the transmission for the spin up bands K_+ and K_- bands, shown in Fig. 6, help in understanding the resonant features of the conductance and polarization results. The transmission for each band is shifted due to the presence of the EuS substrate. The transmission maxima are highlighted with dot symbols in the well bands, as depicted in Fig. 6(a) and (b). For normal incidence, as the gate potential is applied in the central region, the resonant levels (dots) begin to align with the Fermi energy at the leads (marked with a black horizontal line) and, as a consequence, the conductance exhibits a series of sharp and well-defined peaks. As expected, the number and energy distribution of these peaks depend on the well region length, which is a favorable condition to obtain gate-tunable values of spin and valley polarization. It is important to emphasize that the perfect resonant conductance peaks observed in Fig. 6 are obtained only for normal incidence, otherwise, an angle integrated conductance has to be calculated [via Eq. 9], giving broad peaks centered at the resonant energy values. These resonances can be tuned by the gate potentials, generating the corresponding spin- and valley-transport polarizations.

Two relevant situations, for the spin and valley polarization showed in Fig. 7 are highlighted with dashed lines in this plot: (i) a potential at which both spin and valley polarizations are zero (-85.9 meV) and (ii) a potential at which the valley and spin polarizations have opposite signs (-25.4 meV). We investigate how these polarizations depend on the barrier length L and on the potential height U_b , at both energies, as depicted in Fig. 8 (a-d). In the contour plots $U_w = -25.4$ meV and -85.9 meV for top and bottom panels, respectively. The results suggest that it is possible to obtain zero polarization or highly spin and valley polarized heterostructure depending on the potential well energy, in a wide range of parameter space (U_b, L). It is also observed that, by increasing the barrier potential intensity U_b it is possible to change the spin and valley polarization signs, from positive to negative and vice-versa, at a fixed barrier length,

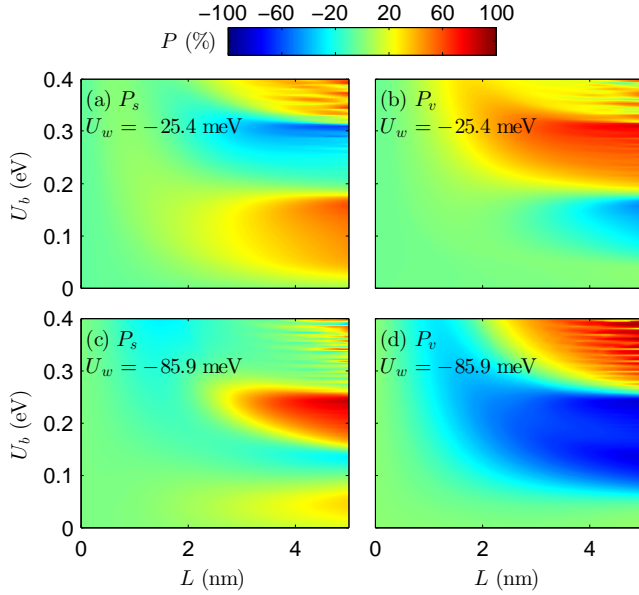


FIG. 8. Spin and valley polarization contour plots as functions of the barrier height U_b and lengths L for the double barrier system at a fixed energy equal to 104.68 meV above the Fermi level. Well length is $d = 30$ nm, well depth for panels(a-b) is $U_w = -25.40$ meV while for panels(c-d) is $U_w = -85.90$ meV.

specially around $L = 4$ nm [see 8 (a) and (d)]. As the barrier potential U_b is increased, the energy distribution of the resonant states in the well region changes, separating and defining these levels in such a way that the resonant tunneling is affected. For some U_b values, the system conducts preferentially by the $\uparrow K_+$ or the $\uparrow K_-$ conductance components promoting, therefore, a sign reversal of the spin and valley polarizations. Finally, for $d = 30$ nm, the optimal parameter space values (U_b, L) at which the maximum valley polarization is obtained, is around $U_b = 200$ meV and for $L > 2.5$ nm.

We further explore the dependence of the valley and spin conductances and polarizations on the quantum well potential U_w and length d . Results for each one of the conductance components, for a double barrier system of length and height $L = 3$ nm and $U_b = 300$ meV, respectively, and at a fixed incident electron energy $E = 104.68$ meV above the Fermi level, are presented in Fig. 9 (a-d). The resonant nature of the electronic states of the well are revealed through the parabolic-like features, marking non-zero conductance in the contour plots, as the intensity potential and geometrical dimension of the quantum well are swept. The spin and valley polarization contour plots, depicted in Fig. 9 (e) and (f), respectively, present complex patterns, indicating clearly that drastic changes may occur for a fixed quantum well length as the well potential goes from zero to -100 meV. It is important to notice that, to avoid spurious results, we have calculated in these plots the weighted polarization [36, 47], which is defined as $wP_s = G_{\uparrow(\downarrow)} P_s$ and $wP_v = G_{K(K')} P_v$.

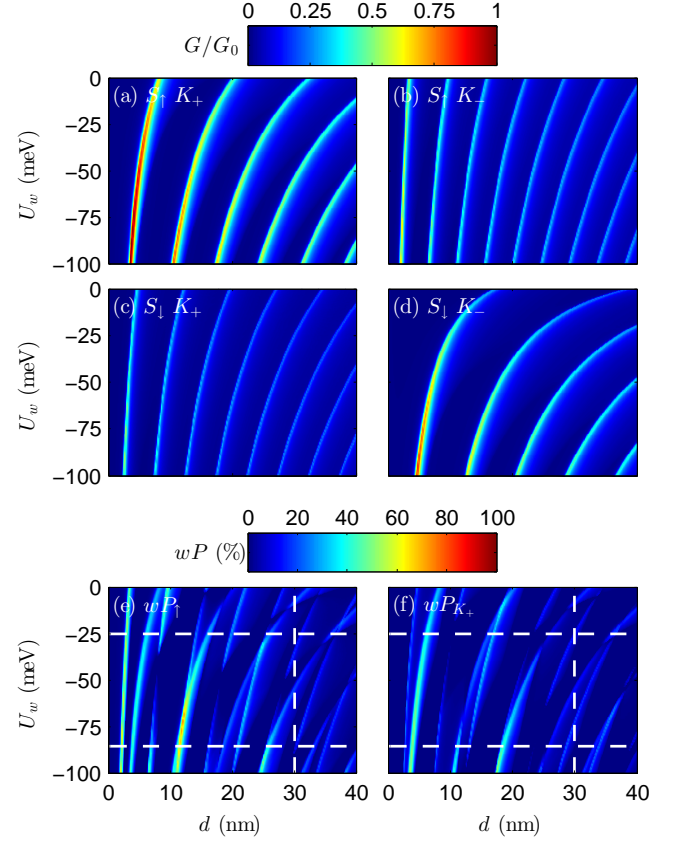


FIG. 9. Spin and valley conductance (a-d) and weighted polarization contour plots (e-f) as functions of the well depth and length, U_w and d , for the double barrier system at a fixed energy of 104.68 meV above the Fermi level. Barrier length and height are $L = 3$ nm and $U_b = 300$ meV, respectively.

C. External AC-field

As previously mentioned, we address the possibilities of getting interesting spin and valley filter scenarios for WSe₂ devices by properly exposing the system to a time-dependent radiation. The external potential can be a laser or a time dependent gate voltage, with frequency $\hbar\omega$ and amplitude potential eV_{ac} , applied to the whole system. In order to obtain modulations of the heterostructure transport response, we have explored different time dependent potential parameters ($\hbar\omega, eV_{ac}$). The main features obtained for a double barrier device, under the oscillating potential, are illustrated in Fig. 10 via spin and valley conductance [(a) and (b)] and polarization [(c)-(f)] contour-plots in the mid-infrared (between 413 - 24.8 meV) and far-infrared or Terahertz (between 24.84 - 1.24 meV) frequency range, and as a function of the amplitude potential eV_{ac} . The analyzed structure has a barrier height $U_b = 300$ meV and length $L = 3$ nm, whereas the quantum well geometry is defined by a well length $d = 30$ nm and two potential depths $U_w = -25.40$ meV and -85.90 meV, in the left and right panels, respec-

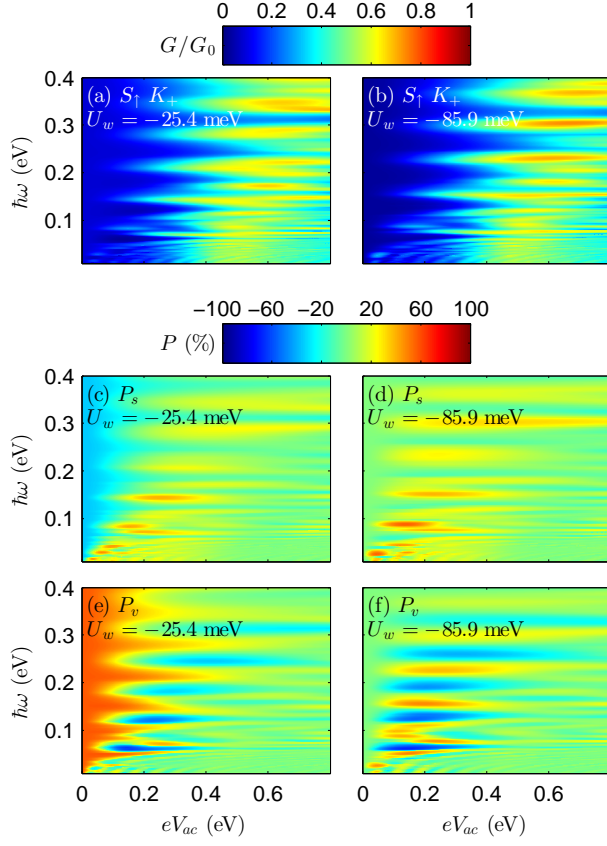


FIG. 10. Spin and valley conductance and polarization contour plots as functions of the ac-field frequency $\hbar\omega$ and power eV_{ac} , for the double barrier system in the FAR-IR frequency range. Parameters: barrier and well lengths $L = 3$ nm and $d = 30$ nm, barrier height $U_b = 300$ meV. Well depth for the left (a,c,e) and right (b,d,f) panels, are $U_w = -25.4$ meV and $U_w = -85.9$ meV, respectively.

tively. These potential values are marked with dashed white lines in weighted spin polarization ωP_{\uparrow} and valley polarization ωP_{K+} of Fig. 9 (e) and (f).

The spin and valley resolved conductances (Fig. 10 (a) and (b)) show that, by applying an oscillating potential to the system, with a radiation amplitude $0 < eV_{ac} < 0.8$ eV, both conductance components become different to zero, with an oscillating behavior as the frequency increase. This means that, due to the presence of the time dependent ac-field, the effective modulation of the electronic wavefunction quantum phase promotes the resonant tunneling in the double barrier heterostructure. Actually, variations up to 70% are noticed at particular potential amplitudes and frequencies.

Similar features are observed in the valley and spin polarization maps, considering the same two values of the potential well U_w , as depicted in the contour plots of Fig. 10 (c-f). For $U_w = -25.4$ meV and $U_w = -85.9$ meV, the spin polarization shows smooth and periodic modulations of its maximum value as the ac-field frequency is increased. However, there are narrow frequency

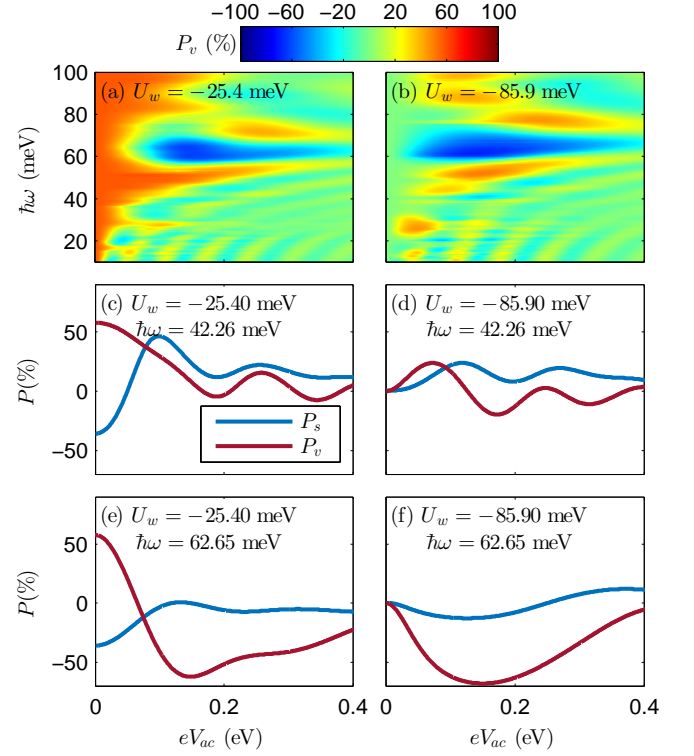


FIG. 11. (a-b) Zoom of the valley polarization contour plots mapped in Fig. 10(e-f) for $U_w = -25.4$ meV and -85.9 meV, respectively. (c-f) Valley and spin polarization results as a function of the ac-field power for the same double barrier system described in the previous figure: barrier length $L = 3$ nm and height $U_b = 300$ meV, well length $d = 30$ nm. The well depth are $U_w = -25.40$ meV (left panels) and -85.90 meV (right panels). In all panels $E_F = 849.98$ meV and an ac-field frequency $\hbar\omega = 42.26$ meV and 62.64 meV, as marked in each panel.

ranges [orange regions in panels (c) and (d)] at which high spin polarization are observed, for different ac-field amplitude. This is more evident for a deeper well potential ($U_w = -85.9$ meV) when more resonant states are allowed into the conductor region, and in the terahertz frequency range, up to 144 meV. For the valley polarization, at $U_w = -25.4$ meV, as the ac-field amplitude is turned on and increased, it is possible to switch from K_+ to K_- valley filter, revealed by the sequence of orange and blue color in the contour plots of panel (e), for a fixed ac-field frequency. Also, considering the potential well $U_w = -85.9$ meV, the system is moved from zero-spin and valley polarizations to $\pm 20\%$ and $\pm 60\%$ spin and valley polarizations, respectively, depending on the far-IR radiation frequency.

These valley switch polarization features are highlighted in the zoom presented in Fig. 11 (a-b), where the laser frequency and potential amplitude were constraint to smaller ranges. Some two-dimensional cuts for the valley and spin polarizations as a function of the ac-field amplitudes are presented in Fig. 11 (c-f), for fixed

quantum well potential and frequency values, as its is indicated in the panels. Actually, by adjusting the ac-field potential, a variety of filter regimes may be achieved, which transforms the double quantum well geometry as a promising platform to reveal the spin and valley filtering behavior of WSe₂ monolayers.

IV. SUMMARY

In this work, we have investigated the spin and valley transport properties of a WSe₂ monolayer placed on top of a ferromagnetic insulator. Single and double barrier heterostructures were explored. By applying external potentials to the system, we have shown that the systems can be used as efficient valley and spin filter devices and how the polarized transport properties depend on the gate-potential intensities and geometrical configuration. We believe that the combination of heterostructured TMD geometries and appropriated gate potentials, proposed in our work, allows to control the resonant tuning provided by the state alignment with the electronic carrier bands. We have found that double barrier structures are more appropriated to valley and spin filters, due to the resonant tunneling, compared with single barrier systems. Additionally, we investigate how the spin and valley polarizations are modified when an ac-field is applied to the system. The radiation field allows tuning both polarizations in a wide range of device geometries, radiation intensities and frequencies, especially in the terahertz range. Inversion of the spin and valley polarizations signal are found possible by changing the laser frequency for fixed power amplitudes. The possibility of spin and valley polarization inversion was not addressed in other works and may be considered as an advantage proposal. Our results suggest that 2D WSe₂ heterostructures are good candidates to provide spin and valley dependent transport and can drive experimental efforts in order to probe spin and valley polarized currents.

V. ACKNOWLEDGMENTS

This work was partially financed by Fondecyt, Grants 1180914 and 1201876 of Chile. AL would like to thanks partial support from FAPERJ (grant E-26/202.567/2019), CNPq, and INCT de Nanomateriais de Carbono.

Appendix A

A Hamiltonian like the one described by Eqs. (1, 2, 4, 5) can always be written in the following form

$$H = \begin{pmatrix} \Delta_c & \hbar v k_- \\ \hbar v k_+ & \Delta_v \end{pmatrix}. \quad (\text{A1})$$

In our model $\Delta_c = S_z(\eta\lambda_c + B_c) + U(x) + m/2$, $\Delta_v = S_z(\eta\lambda_v - B_v) + U(x) - m/2$, $k_{\pm} = \eta k_x \pm i k_y$, v is the Fermi velocity and $\eta = \pm 1$ is the valley index. Note that $\hbar^2 v^2 k_+ k_- = (\hbar v k)^2 = c_k^2$.

A straight forward diagonalization of the low energy Hamiltonian defined by eq. (A1) leads to the following spinor for an incident electron in the conduction band

$$V_{S_z, \pm}^{\eta} = \frac{1}{D_k} \begin{pmatrix} \eta c_k e^{-i\eta\theta} \\ b_k \end{pmatrix}, \quad (\text{A2})$$

where $b_k = \sqrt{\Delta_-^2 + c_k^2} - \Delta_-$, $D_k = \sqrt{c_k^2 + b_k^2}$ and $2\Delta_- = \Delta_c - \Delta_v$.

Considering the invariance in the y direction and the structure shown in Fig. 1 the wave functions for the double barrier system are

$$\Psi_I(x, y) = \left[\frac{e^{ik_x x}}{D_k} \begin{pmatrix} \eta c_k e^{-i\eta\theta} \\ b_k \end{pmatrix} + r_{\eta, S_z} \frac{e^{-ik_x x}}{D_k} \begin{pmatrix} \eta c_k e^{-i\eta(\pi-\theta)} \\ b_k \end{pmatrix} \right] e^{ik_y y}, \quad (\text{A3})$$

$$\Psi_{II}(x, y) = \left[A \frac{e^{iq_x x}}{D_q} \begin{pmatrix} \eta c_q e^{-i\eta\varphi} \\ b_q \end{pmatrix} + B \frac{e^{-iq_x x}}{D_q} \begin{pmatrix} \eta c_q e^{-i\eta(\pi-\varphi)} \\ b_q \end{pmatrix} \right] e^{ik_y y}, \quad (\text{A4})$$

$$\Psi_{III}(x, y) = \left[C \frac{e^{iw_x x}}{D_w} \begin{pmatrix} \eta c_w e^{-i\eta\phi} \\ b_w \end{pmatrix} + D \frac{e^{-iw_x x}}{D_w} \begin{pmatrix} \eta c_w e^{-i\eta(\pi-\phi)} \\ b_w \end{pmatrix} \right] e^{ik_y y}, \quad (\text{A5})$$

$$\Psi_{IV}(x, y) = \left[E \frac{e^{iq_x x}}{D_q} \begin{pmatrix} \eta c_q e^{-i\eta\varphi} \\ b_q \end{pmatrix} + F \frac{e^{-iq_x x}}{D_q} \begin{pmatrix} \eta c_q e^{-i\eta(\pi-\varphi)} \\ b_q \end{pmatrix} \right] e^{ik_y y}, \quad (\text{A6})$$

$$\Psi_V(x, y) = t_{\eta, S_z} \frac{e^{ik_x x}}{D_k} \begin{pmatrix} \eta c_k e^{-i\eta\theta} \\ b_k \end{pmatrix} e^{ik_y y}, \quad (\text{A7})$$

where the coefficients D_q , b_q , D_w and b_w are defined in the same way as D_k and b_k , but with the corresponding parameters accordingly to Fig. 1.

The transmission probability is found by matching the wave functions at the interfaces; at $x = 0$ we have $\Psi_I(0) = \Psi_{II}(0)$ which is written into two equations

$$\frac{\eta c_k e^{-i\eta\theta}}{D_k} + r_{\eta, S_z} \frac{\eta c_k e^{-i\eta(\pi-\theta)}}{D_k} = A \frac{\eta c_q e^{-i\eta\varphi}}{D_q} + B \frac{\eta c_q e^{-i\eta(\pi-\varphi)}}{D_q} \quad (\text{A8})$$

$$\frac{b_k}{D_k} + r_{\eta, S_z} \frac{b_k}{D_k} = A \frac{b_q}{D_q} + B \frac{b_q}{D_q}. \quad (\text{A9})$$

At $x = L$ we have $\Psi_{II}(L) = \Psi_{III}(L)$, and similarly

$$A \frac{\eta c_q e^{-i\eta\varphi}}{D_q} e^{iq_x L} + B \frac{\eta c_q e^{-i\eta(\pi-\varphi)}}{D_q} e^{-iq_x L} = C \frac{\eta c_w e^{-i\eta\phi}}{D_w} e^{iw_x L} + D \frac{\eta c_w e^{-i\eta(\pi-\phi)}}{D_w} e^{-iw_x L} \quad (\text{A10})$$

$$A \frac{b_q}{D_q} e^{iq_x L} + B \frac{b_q}{D_q} e^{-iq_x L} = C \frac{b_w}{D_w} e^{iw_x L} + D \frac{b_w}{D_w} e^{-iw_x L}. \quad (\text{A11})$$

At $x = L + d$, $\Psi_{III}(L + d) = \Psi_{IV}(L + d)$ and we obtain

$$C \frac{\eta c_w e^{-i\eta\phi}}{D_w} e^{iw_x(L+d)} + D \frac{\eta c_w e^{-i\eta(\pi-\phi)}}{D_w} e^{-iw_x(L+d)} = E \frac{\eta c_q e^{-i\eta\varphi}}{D_q} e^{iq_x(L+d)} + F \frac{\eta c_q e^{-i\eta(\pi-\varphi)}}{D_q} e^{-iq_x(L+d)} \quad (\text{A12})$$

$$C \frac{b_w}{D_w} e^{iw_x(L+d)} + D \frac{b_w}{D_w} e^{-iw_x(L+d)} = E \frac{b_q}{D_q} e^{iq_x(L+d)} + F \frac{b_q}{D_q} e^{-iq_x(L+d)}. \quad (\text{A13})$$

And finally at $x = L + d + L$, $\Psi_{IV}(2L + d) = \Psi_V(2L + d)$ and we get

$$E \frac{\eta c_q e^{-i\eta\varphi}}{D_q} e^{iq_x(2L+d)} + F \frac{\eta c_q e^{-i\eta(\pi-\varphi)}}{D_q} e^{-iq_x(2L+d)} = t_{\eta, S_z} \frac{\eta c_k e^{-i\eta\theta}}{D_k} e^{ik_x(2L+d)} \quad (\text{A14})$$

$$E \frac{b_q}{D_q} e^{iq_x(2L+d)} + F \frac{b_q}{D_q} e^{-iq_x(2L+d)} = t_{\eta, S_z} \frac{b_k}{D_k} e^{ik_x(2L+d)}. \quad (\text{A15})$$

The $r_{\eta, S_z}^{\text{Double}}$ and $t_{\eta, S_z}^{\text{Double}}$ coefficients are obtained by solving the equation system defined by Eq. A8 to Eq. A15, resulting in the following expression for the transmission coefficient:

$$F_2 = -4i \sin(w_x d) (\cos(2Lq_x) + \cos(2\varphi)), \quad (\text{A19})$$

$$t_{\eta, S_z}^{\text{Double}} = \frac{16e^{-2ik_x L} e^{-ik_x d} \cos(\varphi)^2 \cos(\phi) \cos(\theta)}{\xi}, \quad (\text{A16})$$

with the denominator ξ given by

$$F_3 = -4i (\sin(w_x d) + \sin(2q_x L - w_x d)) \cos(\varphi - \phi) \\ + 4i (\sin(w_x d) - \sin(2q_x L + w_x d)) \cos(\varphi + \phi), \quad (\text{A20})$$

$$\xi = F_1 + \left(\frac{c_k b_w}{c_w b_k} + \frac{c_w b_k}{c_k b_w} \right) F_2 + \left(\frac{c_k b_q}{c_q b_k} + \frac{c_q b_k}{c_k b_q} \right) F_3 + \\ \left(\frac{c_q b_w}{c_w b_q} + \frac{c_w b_q}{c_q b_w} \right) F_4 + \left(\frac{c_k c_w b_q^2}{c_q^2 b_k b_w} + \frac{c_q^2 b_k b_w}{c_k c_w b_q^2} \right) F_5. \quad (\text{A17})$$

$$F_4 = -8 \sin(w_x d) e^{iq_x L} \sin(q_x L) \cos(\theta - \varphi) \\ - 8 \sin(w_x d) e^{-iq_x L} \sin(q_x L) \cos(\theta + \varphi), \quad (\text{A21})$$

and

$$F_5 = 8i \sin(w_x d) \sin(q_x L)^2. \quad (\text{A22})$$

where the functions F_i are defined as

$$F_1 = -8i \sin(w_x d) \cos(\theta + \phi) \\ + 8i \sin(w_x d) \cos(\theta - \phi) \\ + 4e^{iw_x d} \cos(2q_x L) \cos(\theta + \phi) \\ + 4e^{-iw_x d} \cos(2q_x L) \cos(\theta - \phi) \\ + 2e^{-iw_x d} e^{-2iq_x L} \cos(\theta + \phi + 2\varphi) \\ + 2e^{iw_x d} e^{-2iq_x L} \cos(\theta - \phi + 2\varphi) \\ + 2e^{-iw_x d} e^{2iq_x L} \cos(\theta + \phi - 2\varphi) \\ + 2e^{iw_x d} e^{2iq_x L} \cos(\theta - \phi - 2\varphi), \quad (\text{A18})$$

For the single barrier heterostructure the wave functions for the zones III and IV must be neglected and d must be set equal to zero. A similar equation system is then obtained. The transmission coefficient of the single barrier, $t_{\eta, S_z}^{\text{Single}}$, is analytically determined, and given by Eqs. (6) and (7).

-
- [1] T. Norden, c. Zhao, P. Zhang, R. Sabirianov, A. Petrou, and H. Zeng, Giant valley splitting in monolayer WS_2 by magnetic proximity effect, *Nat. Commun.* **10**, 4163 (2019).
- [2] J. Qi, X. Li, Q. Niu, and J. Feng, Giant and tunable valley degeneracy splitting in MoTe_2 , *Phys. Rev. B.* **92**, 12, 121403 (2015).
- [3] M. Tahir, P. M. Krstajić, and P. Vasilopoulos, Magnetic and electric control of spin-and valley-polarized transport across tunnel junctions on monolayer WSe_2 , *Phys. Rev. B.* **95**, 23, 235402 (2017).
- [4] H. Li, J. Shao, D. Yao, and G. Yang, Gate-Voltage-Controlled Spin and Valley Polarization Transport in a Normal/Ferromagnetic/Normal MoS_2 Junction, *ACS Applied Materials & Interfaces* **6**, 3, 1759-1764, (2014).
- [5] K. S. Novoselov, A. Mishchenko, A. Carvalho, A. H. Castro Neto, 2D materials and van der Waals heterostructures, *Science* **353**, 6298 (2016).
- [6] Q. H. Wang, K. Kalantar-Zadeh, A. Kis, J. N. Coleman, and M. S. Strano, Electronics and optoelectronics of two-dimensional transition metal dichalcogenides, *Nature Nanotechnology* **7**, 699 (2012).
- [7] S. Manzeli, D. Ovchinnikov, D. Pasquier, O. V. Yazyev and A. Kis, 2D transition metal dichalcogenides, *Nature Reviews Materials* **2**, 17033 (2017), and *all references therein*.
- [8] M. Chhowalla, H. S. Shin, G. Eda, L.-J. Li, K. P. Loh, and H. Zhang, The chemistry of two-dimensional layered transition metal dichalcogenide nanosheets, *Nature Chemistry* **5**, 263 (2013).
- [9] Z. Wang, L. Zhao, K. F. Mak, and J. Shan, Probing the Spin-Polarized Electronic Band Structure in Monolayer Transition Metal Dichalcogenides by Optical Spectroscopy, *Nano Letters* **17**, 740 (2017).
- [10] C. Zhang, Y. Chen, J. K. Huang, X. Wu, L. J. Li, W. Yao, J. Tersoff and C. K. Shih, Visualizing band offsets and edge states in bilayer-monolayer transition metal dichalcogenides lateral heterojunction, *Nat. Comm.* **7**, 10349 (2016).
- [11] X. Xu, W. Yao, D. Xiao, and T.F. Heinz, Spin and pseudospins in layered transition metal dichalcogenides, *Nature Physics* **10**, 343 (2014).
- [12] X. Qian, J. Liu, L. Fu, J. Li, Quantum spin Hall effect in two-dimensional transition metal dichalcogenides, *Science* **346**, 1344 (2014).
- [13] G. B. Liu, W.Y. Shan, Y. Yao, W. Yao, and D. Xiao, Three-band tight-binding model for monolayers of group-VIB transition metal dichalcogenides, *Phys. Rev. B* **88**, 085433 (2013).
- [14] A. J. Pearce, E. Mariani, and G. Burkard, Tight-binding approach to strain and curvature in monolayer transition-metal dichalcogenides, *Phys. Rev. B* **94**, 155416 (2016).
- [15] D. Xiao, G.B. Liu, W. Feng, X. Xu, and W. Yao, Coupled Spin and Valley Physics in Monolayers of MoS_2 and Other Group-VI Dichalcogenides, *Phys. Rev. Lett.* **108**, 196802 (2012).
- [16] H. Li, J. Shao, D. Yao, and G. Yang, Gate-Voltage-Controlled Spin and Valley Polarization Transport in a Normal/Ferromagnetic/Normal MoS_2 Junction, *ACS Appl. Mater. Interfaces* **6**, 1759 (2014).
- [17] M. Tahir, P. M. Krstajic, and P. Vasilopoulos, Zeeman and electric-field control of spin- and valley-polarized transport through biased magnetic junctions on WSe_2 , *EPL*, **118**, 17001 (2017).
- [18] Y. Ominato, J. Fujimoto, and M. Matsuo, Valley-Dependent Spin Transport in Monolayer Transition-Metal Dichalcogenides, *Phys. Rev. Lett.* **124**, 166803 (2020).
- [19] W. Choi, N. Choudhary, G. H. Han, J. Park, D. Akinwande, Y. H. Lee, Recent development of two-dimensional transition metal dichalcogenides and their applications, *Materials Today* **20**, 116 (2017).
- [20] C. Zhou, Y. Zhao, s. Raju, Y. Wang, Z. Lin, M. Chan, and Y. Chai, Carrier Type Control of WSe_2 Field-Effect Transistors by Thickness Modulation and MoO_3 Layer Doping, *Adv. Funct. Mater.* **26**: 4223-4230 (2016).
- [21] H. Tian, M. L. Chin, S. Najmaei, Q. Guo, F. Xia, H. Wang, and M. Dubey, Optoelectronic devices based on two-dimensional transition metal dichalcogenides, *Nano Res.* **9**, 1543 (2016).
- [22] K. F. Mak and J. Shan, Photonics and optoelectronics of 2D semiconductor transition metal dichalcogenides, *Nature Photonics* **10**, 216 (2016).
- [23] J. H. Yu, H. R. Lee, S. S. Hong, D. Kong, H.-W. Lee, H. Wang, F. Xiong, S. Wang, and Y. Cui, Vertical Heterostructure of Two-Dimensional MoS_2 and WSe_2 with Vertically Aligned Layers, *Nano Lett.* **15**, 2, 1031–1035 (2015).
- [24] H. Li, Z. Yin, Q. He, H. Li, X. Huang, G. Lu, D. W. F. Fam, A. I. Y. Tok, Q. Zhang, and H. Zhang, *Small* **8**, 63 (2012).
- [25] A. J. Molina-Mendoza, M. Paur, and T. Mueller, Non-volatile Programmable WSe_2 Photodetector, *Adv. Optical Mater.* **8**, 2000417 (2020).
- [26] R. Lv, J. A. Robinson, R. E. Schaak, D. Sun, Y. Sun, T. E. Mallouk, and M. Terrones, Transition Metal Dichalcogenides and Beyond: Synthesis, Properties, and Applications of Single- and Few-Layer Nanosheets, *Acc. Chem. Res.* **48**, 56 (2015).
- [27] H. R. Gutiérrez, N. Perea-López, A. L. Elías, A. Berkdemir, B. Wang, R. Lv, F. López-Uriás, V. Crespi, H. Terrones, and M. Terrones, Extraordinary Room-Temperature Photoluminescence in Triangular WS_2 Monolayers, *Nano Lett.* **13**, 3447 (2013).
- [28] G. Aivazian, Z. Gong, A. M. Jones, R.-L. Hu, J. Yan, D. G. Mandrus, C. Zhang, D. Cobden, W. Yao, and X. Xu, Magnetic control of valley pseudospin in monolayer WSe_2 , *Nature Phys.* **11**, 148–152 (2015).
- [29] Y. Liu, Y. Gao, S. zhang, J. He, J. Yu, and Z. Liu, Valleytronics in transition metal dichalcogenides materials, *Nano Research* **12**, 2695 (2019).
- [30] B. T. Zhou, K. Taguchi, Y. Kawaguchi, Y. Tanaka, and K. T. Law, Spin-orbit coupling induced valley Hall effects in transition-metal dichalcogenides, *Communications Physics* **2**, 26, (2019).
- [31] M. Buttiker, H. Thomas and A. Pretre, Current partition in multiprobe conductors in the presence of slowly oscillating external potentials, *Zeitschrift fur Physik B Cond. Matt.* **94**, 133 (1994).
- [32] G. Platero and R. Aguado, Photon-assisted transport in semiconductor nanostructures, *Phys. Rep.* **395**, 1 (2004).
- [33] S. Kholer, J. Lehmann, P. Haennggi, Driven Quantum

- Transport on the Nanoscale, Phys. Rep. **406**, 379 (2005).
- [34] B. L. Altshuler and L. I. Glazman, Pumping Electrons, Science **283**, 1864 (1999).
 - [35] C. Kocabas, H. -S. Kim, T. Banks, J. A. Rogers, A. A. Pesetski, J. E. Baumgardner, S. V. Krishnaswamy, and H. Zhang, et.al, Radio frequency analog electronics based on carbon nanotube transistors, PNAS **105**, 1405 (2008).
 - [36] D. Zambrano, L. Rosales, A. Latgé, M. Pacheco, and P. A. Orellana, Photon-assisted transport in bilayer graphene flakes, Phys. Rev. B **95**, 035412 (2017).
 - [37] C. G. Rocha, L. E. F. Foa Torres, and G. Cuniberti, AC transport in graphene-based Fabry-Pèrot devices, Phys. Rev. B **81**, 115435 (2010).
 - [38] C. Rocha, M. Pacheco, L. E. F. Foa Torres, G. Cuniberti, and A. Latgé, Transport Response of carbon-based resonant cavities under time-dependent potential and magnetic fields, EPL **94**, 47002 (2011).
 - [39] L. E. F. Foa Torres, H. L. Calvo, C. G. Rocha, and G. Cuniberti, Enhancing single-parameter quantum charge pumping in carbon-based devices, Appl. Phys. Lett. **99**, 092102 (2011).
 - [40] G. Usaj, P.M. Perez Piskunow, L. E. F. Foa Torres, C. A. Balseiro, Irradiated graphene as a tunable Floquet topological insulator, Phys. Rev. B **90**, 115423 (2014).
 - [41] Z. Yin, H. Li, H. Li, l. jiang, y. Shi, G. Lu, Q. Zhang, X. Chen, and H. Zhang, Single-Layer MoS₂ Phototransistors, ACS Nano **6**, 74 (2012).
 - [42] K. Roy, M. Padmanabhan, S. Goswami, T. P. Sai, G. Ramalingam, S. Raghavan, and A. Ghosh, Graphene-MoS₂ hybrid structures for multifunctional photoresponsive memory devices, Nat. Nanotech. **8**, 826 (2013).
 - [43] R. Cheng, D. Li, H. Zhou, C. Wang, A. Tin, S. Jiang, Y. Liu, Y. Chen, Y. Huang, and X. Duan, Electroluminescence and Photocurrent Generation from Atomically Sharp WSe₂/MoS₂ Heterojunction p-n Diodes, Nano Lett. **14**, 5590 (2014).
 - [44] X.-J. Hao, R. -Y. Yuan, T. Ji, and Y. Guo, Multiphoton process observed in the interaction of microwave fields with the tunneling between superconductor films, J. Appl. Phys. **128**, 154303 (2020).
 - [45] P. K. Tien and J. R. Gordon, Multiphoton Process observed in the interaction of Microwave Fields with the Tunneling between Superconductor Films, Phys. Rev. **129**, 2 (1963).
 - [46] S. Fathipour, P. Paletti, S. K. Fullerton-Shirey, and A. C. Seabaugh, Electric-double-layer p-i-n junctions in WSe₂, Scientific Reports **10**, 12890 (2020).
 - [47] P. A. Orellana, L. Rosales, L. Chico, and M. Pacheco, Spin-polarized electrons in bilayer graphene ribbons, J. Appl. Phys. **113**, 21 (2013).